[17] Detecting Specular Reflections Using Lambertian Constraints

Gavin Brelstaff and Andrew Blake

Department of Computer Science
University of Edinburgh, Edinburgh EH9 3JZ, Scotland, UK

© 1988 IEEE. Reprinted, with permission from *Proceedings of 2nd International Conference on Computer Vision, 1988,* 297-302.

Abstract

Specularities—bright image regions formed by specular reflection—are likely to be mistaken for genuine surface markings by processes that perform photometric analysis, derive motion fields from optical flow or estimate depth from binocular stereo. In addition they can be used to infer surface geometry. This paper describes a scheme for detecting specularities based on a characterisation of Lambertian surfaces. Real surfaces are not simple composites of Lambertian and specular surfaces but evidence suggests that away from specularities they do not deviate from the Lambertian model by more than a factor of 3 or so. This proves adequate to serve as a constraint for specularity detection. Two independent tests identify image regions where the constraint is violated. The detector is shown to performs well on a variety of real images. Applications: improving binocular stereo and inferring surface geometry are described using specularities produced by the detector.

1 Introduction and other work

Specular reflection occurs whenever a glossy surface reflects light incident upon it in a mirror-like fashion. Specularities—bright image regions formed by specular reflection—are useful features for any practical vision system to identify. Once identified they need no longer be mistaken for genuine surface markings by processes that match models to objects [8], derive motion fields from optical flow (see [40]) or estimate depth from binocular stereo [34,35]. They can also be used to infer surface geometry [21,37,2,13,28,5,6]. Here a scheme is described for detecting specularities based on a characterisation of Lambertian (non-specular) surfaces. Although real surfaces are not simple composites of Lambertian and specular surfaces, experimental evidence suggests that they maintain a roughly Lambertian character in regions away from specularities. Constraints derived for Lambertian surfaces are applied to real images and specularities detected in regions where the constraints are found to be violated.

*Current addresses: A. Blake, Dept. Engineering Science, Parks Rd., Oxford. G. Brelstaff, IBM UKSC, Athelstan Ho., St Clement St., Winchester.

Contemporary work on detecting specularities takes an alternative, chromatic approach [18,27]. Colour differences in the specular and non-specular components of the light reflected by certain materials are exploited. A chromatic approach can complement the achromatic (grey-level) approach described here, but only where colour differences exist—i.e. not for most metals nor for white light incident on a grey surface.

Previous work on detecting specularities in achromatic images is provided by Forbus [16]. He applied Ullman's 'S' operator [39] to images containing specularities. However his method fails for specularities that have smooth shading profiles—as produced by curved surfaces [7]. However, the second directional derivative used by the 'S' operator clearly is capable of distinguishing some specularities The "cylinder test" proposed later also makes use of it. The cylinder test provides a practical method to distinguish between smooth Lambertian and smooth specular shading variations. It is one of two independent tests developed to detect specularities. Both tests use the assumption (justified by experimental results) that surfaces maintain a roughly Lambertian character away from specularities. The tests identify regions where constraints that hold for Lambertian surfaces, are clearly violated. These regions are candidate specularities. Each test exploits a different Lambertian characteristic—as summarised below:

Name of test	Operating principle of test
Retinex-based test	Region 'too bright' to be Lambertian
Cylinder test	Peak 'too sharp' to be Lambertian

The detection scheme combines and propagates the evidence from each test to create a map of the specularities in the image. The results show that the scheme successfully detects prominent specularities in a variety of real images. No explicit model of specularities is involved. This is a great advantage because the models of composite specular and matte surface reflection that do exist require a great deal of a priori knowledge of the scene surfaces and lighting before they can be exploited. In fact the reflective properties of many common materials are poorly understood and no useful models exist for them. Before describing the details of both tests, the basis for their underlying assumptions is discussed.

2 Lambertian characteristics of real surfaces

The physical processes involved when real surfaces reflect light are very complicated, even for common materials. Some of the light incident upon a surface is directly reflected at the air-surface interface, while the rest penetrates into the sub-surface layer and may be scattered by particles contained within it. Total reflected light flux combines contributions from both direct reflection and sub-surface scattering. The directional distribution of the light reflected by the two contributing processes can be quite different. A narrow beam of incident light is scattered by the sub-surface over a wide range of directions, while direct reflection directs light back into a narrow beam aligned along the direction of mirror reflection. Direct reflection of a light source creates a specularity when formed into an image. In order to detect specularities the flux due to direct reflection must, in some sense, be separated from that due to sub-surface scattering. So, is it possible to tell apart the flux produced by the two processes and thus detect specularities? As mentioned earlier, colour differences in the flux can sometimes be exploited. This paper considers what can be done with "white" (achromatic) light. One possibility would be to use the available theories of the physical processes to model the amount and directional distribution of the light reflected by a surface and then attempt to fit the model to images. Specularities would be detected where the fitted model requires a significant proportion of direct reflection. However three facts make this approach impractical:

1. For many materials no adequate theory exists. Good models of *direct reflection* exist only for surface of certain roughness [38,3,36,15]. The Lambertian model provides a rough approximation of *sub-surface scattering*— more realistic models applying only in some circumstances [25,11,12,31].

2. Even if a material is adequately modelled a prohibitively large number of fitting parameters are involved. For example the simplest models [25] of sub-surface reflection involve at least five parameters— even more when direct reflection is included.

3. In order to interpret an image in terms of a surface model the precise directional distribution of the illumination is required.

In the absence of theory, the reflective properties of individual materials have been measured. Photometric surface properties are defined in terms of radiance, irradiance and BRDF [32,24]. For a glossy mirror-like surface the BRDF, f_r is small for all pairs of directions except those of mirror-like alignment. For a Lambertian surface it is constant: $f_r = \rho/\pi$ where ρ, known as albedo, is the ratio of the flux reflected to that which is incident. As surfaces absorb some percentage of the incident light without reflecting it ρ has a legal range $(0, 1)$. The simplicity of the Lambertian BRDF makes it a useful standard against which to compare the BRDF's of real surfaces. Naturally, matte surfaces—for which sub-surface scattering is the dominant reflection process, deviate less from this standard than glossy surfaces—which produce large variations in f_r, between mirror-like and other orientations. The specularity detector described in this paper is based on the **assumptions** that:

1. real sub-surface scattering is approximately Lambertian, producing deviations from a constant f_r of at most a factor of 3, except at geometrical conditions for specular reflection.

2. real surfaces are also roughly Lambertian for all directions of incidence and reflection, except at geometrical conditions for specular reflection.

The validity of each assumption is discussed below with reference to data taken from the theoretical and experimental literature. Each graph corresponds to a particular material—plotting the variation in the relative value of the BRDF with angle of reflection θ_r, for a fixed value of the angle of incidence θ_i. For all of the graphs the directions of incidence and reflection lie in the plane containing the local surface normal. If any measurements have been made for a material it is usually in this plane. In any case, when direct reflection acts to divert the BRDF from Lambertian the deviation is most marked in this plane.

Although isotropic sub-surface scattering [25] does not, as one might expect, result in isotropic (Lambertian) reflection, it does to within the approximation provided above—except at glancing angles. The theoretically de-

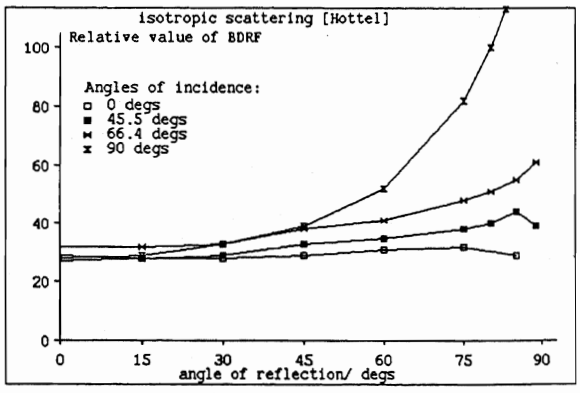

Figure 1: Theoretical prediction of BRDF for an isotropic scatter. A Lambertian surface would produce a horizontal line.

rived graphs in fig 1 show this—only at glancing angles ($\theta_i \geq 70^\circ$ and $\theta_r \geq 70^\circ$, $\theta_i \approx \theta_r$) does the BRDF grow larger—resulting in a considerable deviation from the a constant f_r. However this occurs only at or close to the

geometrical conditions for specular reflection and so does not refute assumption 1. The available measurements of real, near isotropic scatters, e.g: fig 2, confirm the theoretical predictions of fig 1. Sub-surface scattering need

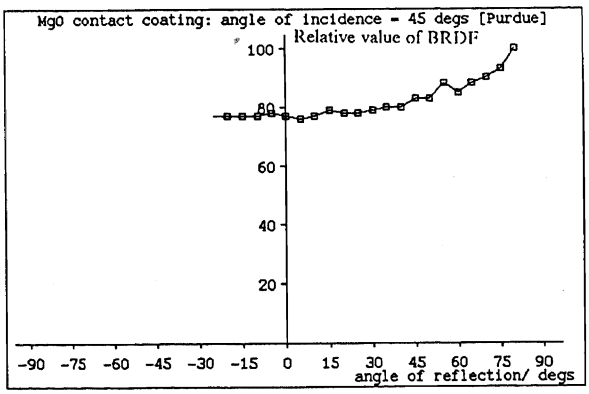

Figure 2: MgO contact coating: $\theta_i = 45°$ [36].

not be isotropic. For the example shown in fig 3 the deviation from constant f_r is by less than a factor of three. If this data is typical then assumption 1 above will be good. In order to address assumption 2 materials that

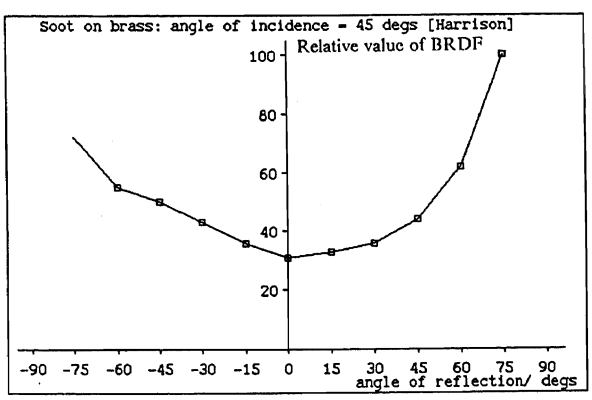

Figure 3: Soot on brass: $\theta_i = 45°$ [20].

reflect light directly must be considered. These materials are of two types:

- Metals which reflect (by electric dipole interaction) almost all incident light directly so that sub-surface scattering is negligible.
- Dielectrics which reflect (by atomic or ionic dipole interaction) some incident light directly—the rest penetrates the surface—so that sub-surface scattering can occur.

For metals with smooth surfaces $f_r \sim 0$ except for specular geometry. For dielectrics an additional component due to sub-surface scattering must be considered. Fig 4 illustrates a typical example: porcelain enamel. Here f_r is roughly constant except for the pulse-like peak at the mirror-like orientation. So for both metals and dielectrics with smooth surfaces assumption 2 looks good. The di-

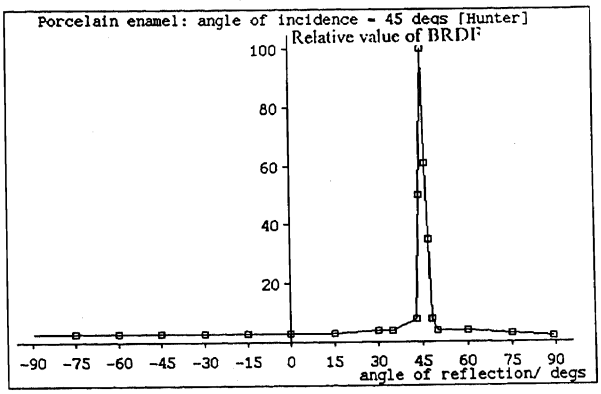

Figure 4: Porcelain enamel: $\theta_i = 45°$ [26].

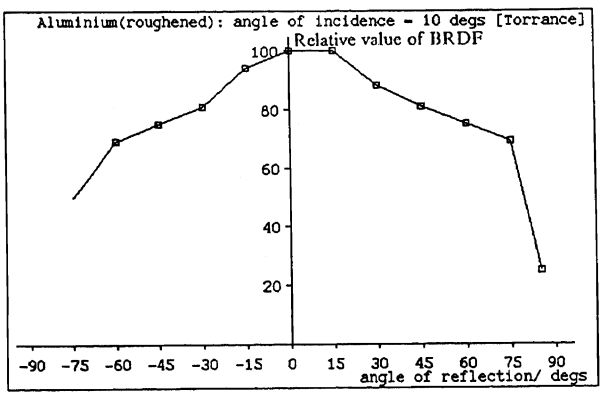

Figure 5: Aluminium (roughened): $\theta_i = 10°$ [38].

rectional distribution of directly reflected light, which is a narrow peak (fig 4) for a smooth surface, becomes a broader peak for a rough surface. The data for roughened aluminium—fig 5—illustrates just how wide the spread can be. The shape of this particular graph is explained by modeling the surface roughness as many micro-facets oriented in many different directions [38]. Although entirely due to direct reflection, the graph in fig 5 has a range that deviates from the Lambertian standard by no more than that of sub-surface scatterers (e.g. as in fig 3). So no prominent specularities should be formed. However, the graph is typical only of small angles of incidence θ_i. As θ_i increases the graph becomes more pulse-like—see fig 6. When θ_i is large the range of the graph deviates significantly from the Lambertian standard and prominent specularities are produced. The discussion above is of a rough metal surface—dielectric surfaces of similar roughness behave similarly [38]. So, the survey above—encompassing metals and dielectrics, both rough and smooth—suggests that assumptions 1 and 2 above, are good.

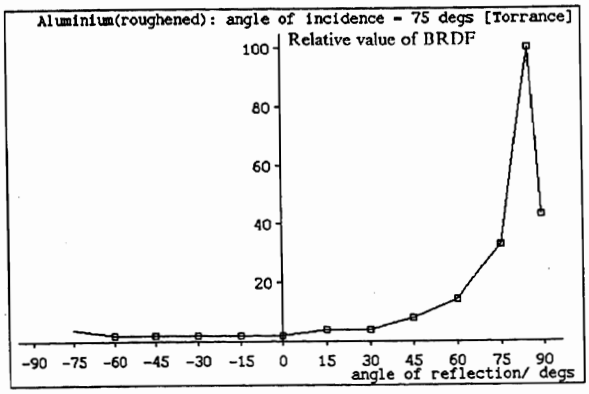

Figure 6: Aluminium (roughened): $\theta_i = 75°$ [38].

3 Lambertian constraint on irradiance

The general specification of a material's reflective properties provided by the BRDF is independent of any considerations of the illumination. The image irradiance registered by a camera depends on the illumination as well as on the BRDF of the surface. Illumination varies across a scene. The general relationship between image irradiance, E, and the BRDF, f_r, for a given imaged point is [24]:

$$E = \int_{\omega_i} f_r L_i \cos\theta_i d\omega_i, \qquad (1)$$

where the illumination at the point is fully specified by L_i: the directional distribution function of the incident radiance. The integral is over all directions encompassed by the solid angle of the incident beam ω_i. For extended or multiple illuminants it is often necessary to integrate over the entire hemisphere above the surface. The variations in E due to L_i and f_r are not, in general, separable—so that the image irradiance equation (1) is very difficult to exploit. However, for Lambertian surfaces $f_r = \rho/\pi$, so equation (1) simplifies:

$$E = \rho I; \quad I = (1/\pi) \int_{\omega_i} L_i \cos\theta_i d\omega_i, \qquad (2)$$

so image irradiance can be separated into the product of albedo ρ and I: a term that quantifies the net illumination falling at the surface point. I and ρ both vary with location $\mathbf{x}$ of the point in the image. I also depends on the local surface orientation (conveniently specified by the direction of the surface normal $\hat{\mathbf{n}}$). Equation (2) can be written:

$$E(\mathbf{x}) = R_L(\hat{\mathbf{n}}(\mathbf{x}), \mathbf{x}) = \rho(\mathbf{x}) I(\hat{\mathbf{n}}(\mathbf{x}), (\mathbf{x})), \qquad (3)$$

where R_L is an extension of the concept of the reflectance map familiar to computer vision. In this form the image irradiance equation is amenable to analysis in terms of the three component variations: $\rho(\mathbf{x})$, I with respect to $\hat{\mathbf{n}}$ and I with respect to $\mathbf{x}$. Any R_L that corresponds to realistic natural matte surface reflection is constrained. An upper bound on the dynamic range of R_L is established below by considering realistic limits on natural variations in $\rho(\mathbf{x})$ and $I(\hat{\mathbf{n}}, \mathbf{x})$.

3.1 Realistic dynamic range of I with respect to $\hat{\mathbf{n}}$ for natural illumination

Perfectly collimated illumination does not prevail in natural everyday circumstances. It can only be achieved in a dark-room. Light may seem to be collimated in some natural circumstances, e.g. spot-light illumination, but the collimation is not perfect. The inter-reflection of light between the surfaces of the scene adds a small non-zero component to the illumination incident along every direction. In terms of the L_i function: it is no longer non-zero only for the direction of collimation—it is non-zero everywhere. The non-zero component is often referred to as the ambient light and it accounts, very roughly for 1/3rd of the net illumination [33]. In computer graphics images with a remarkably natural appearance have been simulated using a simple illumination model incorporating a constant ambient component [14]. The "collimated plus ambient" illumination model is:

$$I(\hat{\mathbf{n}}, \mathbf{x}) = I_0(\mathbf{x}) \left(1/3 + (2/3)\max(0, \hat{\mathbf{n}} \cdot \hat{\mathbf{L}})\right), \qquad (4)$$

where $\hat{\mathbf{L}}$ is the direction of collimation and I_0 is the net illumination along $\hat{\mathbf{L}}$. In this case $I(\hat{\mathbf{n}}, \mathbf{x})$ has a dynamic range of 3 over all surface orientations at a given $\mathbf{x}$. This collimated model is a worst case—for multiple sources or an extended source (e.g. a large window or the sky) the dynamic range is the same if not less. Both multiple and extended sources serve to distribute the net incident illumination over a wider range of directions. Informal experiments with a spot photometer, indoors under various lighting conditions confirm that **3** is a reasonable value.

3.2 Realistic dynamic range of $\rho(\mathbf{x})$ for natural materials

The legal range of albedo is $\rho \in (0, 1)$. Real surfaces away from specular geometries exhibit an effective albedo. In practice real dielectrics are neither perfect reflectors nor perfect absorbers and their effective albedo lies in a restricted range $\rho \in (\rho_{min}, \rho_{max})$. In operating circumstances the dynamic range of effective albedo in a scene ρ_{max}/ρ_{min} is found to have an upper bound of roughly 10. Table 1 summarises the available data. Normal-hemispherical reflectance $\rho(0; 2\pi)$ provides a useful estimate of effective albedo [7]. By simply taking the maximum and minimum values of $\rho(0; 2\pi)$ in the table a very large dynamic range: $98\%/0.3\% \sim 3000$ is obtained. When some of the materials: chemical powders, carbon black and black velvet are discounted—upon the basis that they are very rarely encounted—a much lower value prevails: $90\%/5\% \sim 18$. In fact it seems safe to use a still lower value, **10** for commonly encountered materials.

Material	$\rho(0;2\pi)$	References
Pure powders (e.g. MgCO3)	98–80%	[17]
Sugar, Flour, Talc., Starch	90–80%	[17,22]
White paint, papers, cloth	80–60%	[17,22,36,19]
Coloured pigments:	80–8%	[17]
..Chrome yellow	80%	
..Ultramarine	8%	
Building Materials:	90–9%	[17,22]
..Clays	90–11%	
..Concrete	35–9%	
..Slates	20–10%	
..Roofing Materials	78–11%	
..Bricks	64–11%	
..Pine Wood	40%	
Peach, Pear (ripe or green)	40–20%	[22]
Coloured porcelain-enamel	70–20%	[22]
Black papers	6–5%	[22]
Black velvet	0.4%	[22]
Carbon black in oil	0.3%	[22]

Table 1: Measured values of $\rho(0;2\pi)$ for various dielectrics.

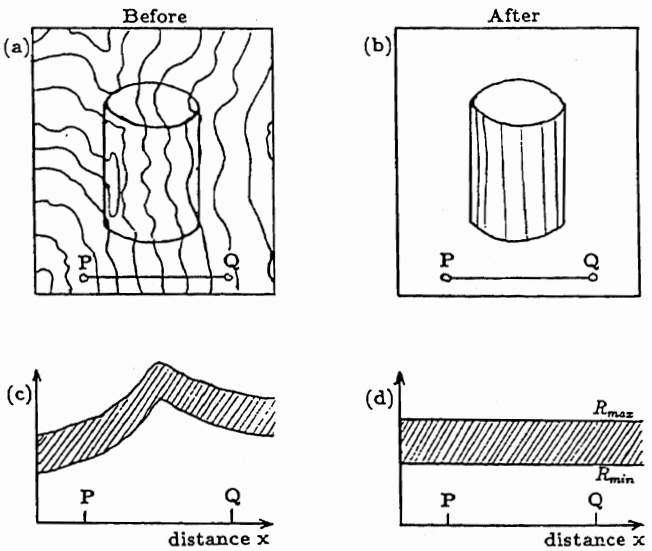

Figure 7: (a) Before retinex pre-processing, spatial variations in net illumination are present in the image irradiance signal. (b) After processing any gradual variations have been eliminated. (c) Before processing, the 30:1 dynamic range constraint does not apply. (d) After processing, it does.

4 The retinex-based test

The retinex-based test is developed to detect those specularities that are 'too bright' to be matte. This test involves *more* than identifying specularities that exceed a certain fixed brightness threshold because the appropriate threshold value varies with the spatial variations of illumination. By considering relative rather than absolute brightness the test copes with the scene-to-scene variations. Variations within a single image are removed by applying a retinex process (fig 7). After removal of spatial variations in illumination $I(\hat{\mathbf{n}},\mathbf{x})$ the dynamic range of image irradiance, for Lambertian-like regions has an upper bound of about **30**, the product of the bounds on $\rho(\mathbf{x})$ and $I(\hat{\mathbf{n}},\mathbf{x})$ (i.e. 10 × 3). Bright regions in an image with a dynamic range exceeding 30 are candidate specularities.

A variety of computational schemes of the retinex are available [29,23]. The implementation used here [9] is correct in its treatment of the image perimeter. Although the retinex is designed to work in a (Mondrian) world without the shading gradients introduced by surface curvature, Land [30] shows that it usefully eliminates illumination variations present in images of real curved surfaces. However, as the retinex cannot distinguish the smaller shading gradients from those due to gradual changes in the illumination level, it is apt to remove them too. This somewhat reduces the power of the test. Removal of gradual changes is done by gaussian filtering [7].

5 The cylinder test

Specularities can often be distinguished from Lambertian shading by the sharpness of their irradiance peaks. The cylinder test quantifies just how sharp a peak must be before the Lambertian interpretation can be discounted. It does this by placing an upper bound U, on the 2nd derivative of irradiance, $D(x_P)$ at the peak location, x_P along the direction of any 1-D profile through an elongated bright region (blob). Where ever $D(x_P) > U$ a specularity is detected. Very narrow profiles are excluded—they might simply be due to thin white matte lines on a dark background. A method akin to that of Asada and Brady [1] is used to extract suitable profiles [7]. The appropriate value of threshold U is computed for a given profile using its dimensions. By a worst case analysis [7], the value can be shown to be

$$U = E(x_P)/(r_1 r_2), \tag{5}$$

where $E(x_P)$ is peak irradiance and r_1 and r_2 are the image distances from the flanking edges of the profile. Establishing this expression requires two assumptions: that albedo is uniform between flanking edges[23] and the surface is locally approximately cylindrical. The second assumption is not as arbitrary as it might seem: an elongated blob is, in itself, a strong indication of a local cylindrical surface. And since the test requires only a bound on, rather than an accurate estimate of $D(x_P)$, it is robust to modest curvature along the spine of the blob. This bound holds *for all* viewer-source geometries, cylinder radii, levels of ambient illumination and portions of a cylinder.

6 Results and applications

Fig 9 show how the specularity detector performs on a set of real images. Each (256x256; 8-bit grey-level) image was acquired from a Link-Electronics 109 vidicon camera. Grey-level was approximately proportional to image irradiance. The signal's (~6 bit) dynamic range was just enough to apply the retinex-based test. Edge maps—used to initiate the profile extraction paths—were obtained using a Canny operator (width $\sigma = 1$ pixel) followed by hysteresis thresholding [10].

Both the retinex-based and cylinder tests provide strong evidence for specularities, but only mark local maxima in image irradiance. To obtain descriptions of the entire specular blob surrounding any maximum the evidence is propagated outwards. A simple but effective method of achieving this is to apply the following process at each maximum where evidence exists:

- Mark the location of the maximum inside the specular blob.
- Recursively apply the same process at any adjacent pixels which are not on the blobs edge contour (as marked in the edge map) and at which the image irradiance exceeds 2/3rds the peak value.

Although fairly arbitrary, this method produces adequate specularity maps corresponding to the maxima at which evidence was found (see fig 9). A more principled approach might fit quadratic patches to the irradiance surface of each specular blob in order to determine the extent of each blob.

The results show that both tests can and do detect genuine specularities. Neither test detects all the genuine specularities in any of the images but importantly neither test marks any false positives. On most occasions the evidence is satisfactorily propagated from the local maxima into the surrounding blobs. Occasionally it is propagated too far: Barring this minor problem, the scheme successfully combines the evidence provided by the tests to create a specularity map. However, at least one genuine specularity is missed in each test image so there is room for improvement. The specularities that are missed are often both too dim for the retinex-based test and too narrow for the cylinder test—e.g. on the left spoke in fig 9 (a). At a higher resolution they might well be detected. Once detected, both the monocular shape and the stereoscopic disparity of a specularity can be used to infer local surface shape as described in the accompanying paper [6]. Specularities should not be used as features for estimating surface depth—their apparent depths are not on the surface. Binocular stereo is improved if specularities are excised before matching and estimating the depth of surface features. Fig 8 shows how excising the detected specularity improves the depth estimated by the PMF stereo algorithm [35]. The fragmentation of the smooth surface is eliminated.

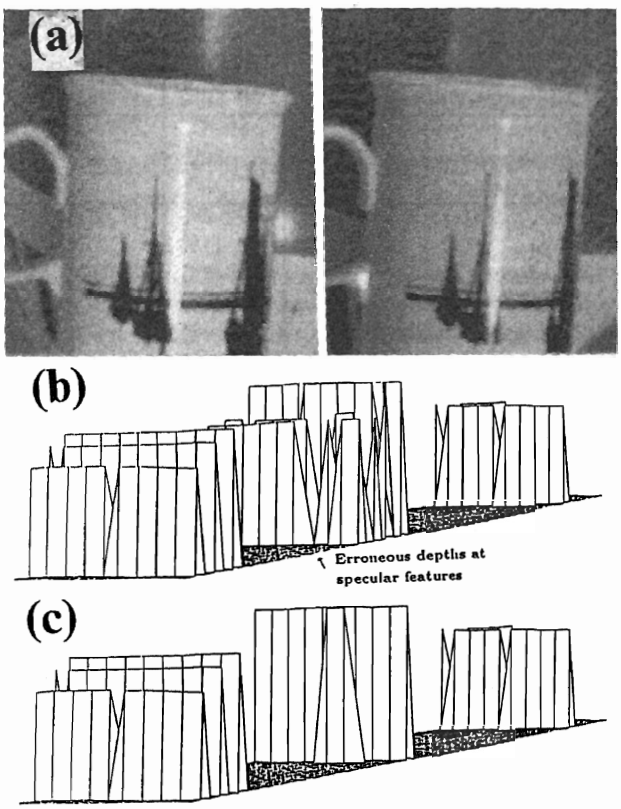

Figure 8: (a) A stereo pair of images (aligned for cross-eyed fusion). Surface plots of part of the sparse depth map from the previous figure, (b) before and (c) after excising the detected specular features.

Acknowledgements

This work was supported by SERC grant GR/D 1439.6, by the University of Edinburgh, by the Royal Society of London's IBM Research Fellowship (for AB) and by the IBM/SERC CASE Studentship (for GB). Thanks to Stephen Pollard at AIVRU, Sheffield for images. We are very grateful to Andrew Zisserman and Constantinos Marinos for helpful discussions.

References

[1] Asada H. and Brady J.M., The Curvature Primal Sketch, *IEEE Trans. PAMI*, 8, 1, (1986), 2-14.

[2] Babu M.D.R., Lee C-H. and Rosenfeld A., Determining Plane Orientation From Specular Reflectance, *Pattern Recognition*, 18, 1, (1985), 53-62.

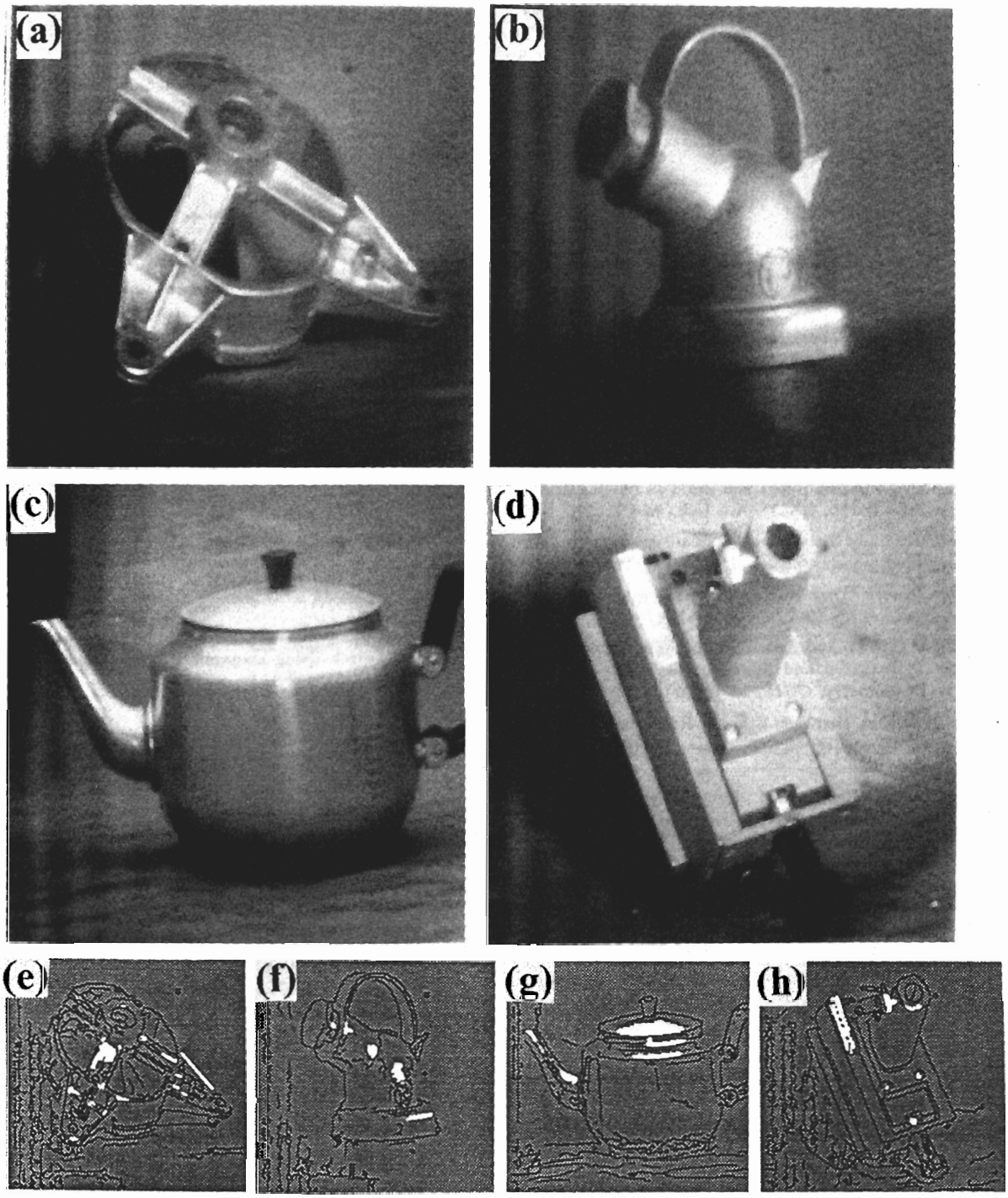

Figure 9: (a)–(d): Series of four real images. (e)–(h): The corresponding series of detected specularities—marked in white (edges in black).

[3] Beckmann P. and Spizzichino A., *The Scattering of Electromagnetic Waves from Rough Surfaces*, MacMillan, New York, (1963).

[4] Billmeyer F.W., Lewis D.L. and Davidson J.G., Goniophotometry of Pressed Barium Sulphate, *Color Engineering, May/June*, (1971) 31-36.

[5] Blake A., Specular Stereo, *Proc. IJCAI-85*, 2, (1985), 973-976.

[6] Blake A. and Brelstaff G.J., Geometry from Specularity, *Proc. 2nd ICCV*, Florida, (1988).

[7] Brelstaff G.J., *Inferring Surface Shape from Specular Reflections*, Ph.d. Thesis, Dept. Comp. Sci., University of Edinburgh (1988).

[8] Bolle R.M. and Cooper D.B., Baysian Recognition of Local 3-D shape by Approximating Image Intensity Functions with Quadric Polynomials, *IEEE Trans. PAMI*, 6, 4, (1984), 418-429.

[9] Brelstaff G.J. and Blake A., Computing Lightness, *Pattern Recognition Letters*, 5, 129-138, (1987).

[10] Canny J.F., *Finding Edges and Lines in Images*, Masters Thesis, AI-TR 720, (1983), A.I. Lab., M.I.T.

[11] Chylek P., Light Scattering by small particles in an absorbing medium, *J. Opt. Soc. Am.* 67, 4, (1977), 561-563.

[12] Chylek P. and Wiscombe W.J., Mie Scattering between any two angles, *J. Opt. Soc. Am.* 67, 4, (1977), 572-573.

[13] Coleman E.N.Jr. and Jain R., Obtaining 3-Dimensional Shape of Textured and Specular Surfaces Using Four-Source Photometry, *CGIP*, 18, (1982), 309-328.

[14] Cook R.L. and Torrance K.E., A Reflectance Model for Computer Graphics, *ACM Trans. on Graphics*, 1, 1, (1982), 7-24.

[15] Elson J.M and Bennet J.M., Relation between the angular dependences of scattering and the statistical properties of optical surfaces, *J. Opt. Soc. Am.*, 69, 1, (1979), 31-47.

[16] Forbus K., *Light Source Effects* A.I. Memo 422, (1977), A.I. Lab., M.I.T.

[17] Forsythe W.E., *Smithsonian Physical Tables*, 9th ed., (1954), 549-559.

[18] Gershon R., Jepson A.D. and Tsotsos J.K., The Use of Color in Highlight Identification, *Proc. 1st ICCV*, London, (1987), 161-170.

[19] Gubareff G.G., Janssen J.E. and Torbourg R.H., *Thermal Radiation Properties Survey: A Review of the Literature*, Honeywell Research Center, Minneapolis, USA, (1960).

[20] Harrison V.G.W., *Definition and Measurement of Gloss*, Monograph, The Printing and Allied Trades Research Assoc. (1945).

[21] Healey G., and Binford T.O., Local shape from specularity, *CVGIP*, 42, (1988), 62-86.

[22] Hodgman C.D., *Handbook of Chemistry of Physics*, 32nd Ed, (1950-51), 2443-2445.

[23] Horn B.K.P., Determining Lightness from an Image, *CGIP*, 3 (1974) 277-299.

[24] Horn B.K.P. and Sjoberg R.W., Calculating the reflectance map, *Applied Optics*, 18, 11, (1979), 1770-1779.

[25] Hottel H.C. and Sarofim A.F., *Radiative Transfer*, McGraw-Hill, 1967.

[26] Hunter R.S., Methods of determining gloss, *J. Res. Nat. Bur. Std.*, 18, (1937) 19-39.

[27] Klinker G.J., Shafer S,A., and Kanade T., Using a color reflection model to separate highlights from object color, *Proc. 1st ICCV*, London, (1987) 145-150.

[28] Koenderink J.J. and van Doorn A,J., Photometric invariants related to solid shape, *Optica Acta*, 27, 7, (1980), 981-996.

[29] Land E.H. and McCann J.J., Lightness and Retinex Theory, *J. Opt. Soc. Am.*, 61, 1, (1971), 1-11.

[30] Land E.H., Recent advances in retinex theory and some implications for cortical computation: Color vision and natural images., *Proc. Natl. Acad. Sci. U.S.A.*, 80, (1983), 5163-5169.

[31] Mudgett P.S. and Richards L.W., Multiple Scattering Calculations for Technology, *Applied Optics*, 10, 7, (1971), 1485-1502.

[32] Nicodemus F.E., Richmond J.C., Ginsberg I.W., Hsia J.J. and Limperist T., *Geometrical Considerations and Nomenclature for Reflectance* Monograph 160, NBS, Washington D.C., (1977).

[33] Nishita T. and Nakamae E., Continuous Tone Representation of Three-Dimensional Objects Taking Account of Shadows and Interreflection, *SIGGRAPH*, 19, 3, (1985), 23-30.

[34] Ohta Y. and Kanade T., Stereo by Intra- and Inter Scanline Search Using Dynamic Programming, *IEEE PAMI*, 7, 2, (1985), 139-154.

[35] Pollard S., Mayhew J.E.W. and Frisby J.P., PMF: a stereo correspondence algorithm using the disparity gradient limit, *Perception*, 14, (1985), 449-470.

[36] Purdue University, *Thermophysical Properties of Matter*, Vols 7, 8 and 9, Plenum, New York, (1970).

[37] Thrift P. and Lee C-H., Using Highlights to Constrain Object Size and Location, *IEEE Trans. Sys, Man and Cyber.*, 13, 3, (1983), 426-431.

[38] Torrance K.E. and Sparrow E.M., Theory of Off-Specular Reflection From Roughened Surfaces, *J. Opt. Soc. Am.*, 57, 9, (1967), 1105-1114.

[39] Ullman S., On Visual Detection of Light Sources, *Biol. Cybernetics*, 21, (1976), 205-212.

[40] Verri A. and Poggio T., Against Quantitative Optical Flow, *Proc, 1st ICCV*, London, June, (1987), 201-208.